Received: 4 June 2019 | Revised: 18 October 2019 | Accepted: 7 December 2019

DOI: 10.1002/aic.16890

TRANSPORT PHENOMENA AND FLUID MECHANICS

AIChE JOURNAL

Micro-computed tomography for the investigation of stationary liquid–liquid and liquid–gas interfaces in capillaries

Julia Schuler | Norbert Kockmann

Laboratory of Equipment Design, Department of Biochemical and Chemical Engineering, TU Dortmund University, Dortmund, Germany

Correspondence
Julia Schuler, Laboratory of Equipment Design, Department of Biochemical and Chemical Engineering, TU Dortmund University, Dortmund, Germany.
Email: julia.schuler@tu-dortmund.de

Funding information
Deutsche Forschungsgemeinschaft, Grant/Award Number: INST 212/397-1

Abstract

For better understanding and optimization of multiphase flow in miniaturized devices, micro-computed tomography (μCT) is a promising visualization tool, as it is nondestructive, three-dimensional, and offers a high spatial resolution. Today, computed tomography (CT) is a standard imaging technique. However, using CT in microfluidics is still challenging, since X-ray related artifacts, low phase contrast, and limited spatial resolution complicate the exact localization of interfaces. We apply μCT for the characterization of stationary interfaces in thin capillaries. The entire workflow for imaging stationary interfaces in capillaries, from image acquisition to the analysis of interfaces, is presented. Special emphasis is given to an in-house developed segmentation routine. For demonstration purposes, contact angles of water, liquid polydimethylsiloxane, and air in FEP, glass, and PMMA are determined and the influence of gravity on interface formation is discussed. This work comprises the first steps for a systematic 3D investigation of multiphase flows in capillaries using μCT.

KEYWORDS

contact angle, interfaces, micro-computed tomography, microfluidics

1 | INTRODUCTION

In the field of process engineering, process intensification via miniaturization has attracted much interest since performing unit operations on a small scale allows overcoming mass transfer limitations, rapid mixing, high surface to volume ratios, and thus, safer processes.[1] Process performance in miniaturized equipment, such as internal mixing or residence time distribution, can be further enhanced by adding a second, immiscible fluid to the single-phase flow, such that a segmented flow pattern, like slug flow or bubbly flow, arises.[2] In segmented flow, recirculation of the fluid within the segments enhances mixing.[2] The shape of the fluid–fluid interfaces highly affects the performance of multiphase flow in miniaturized channels and ducts.[3] The investigation of multiphase interfaces is by no means trivial since non-intrusive measurement techniques are desired. Common approaches to investigate multiphase mini- and microfluidics rely on image acquisition using optical cameras and therefore depend on good optical access. However, such approaches are disadvantageous, especially when optical access is limited or disturbed by optical diffraction.

Apart from conventional 2D imaging using optical cameras, X-ray based computed tomography (CT) became an important tool allowing nondestructive 3D investigation in different fields. For more than two decades, X-ray based CT is used for visualizing liquid–gas distribution resulting from fluid flow in conventional equipment. It enabled the investigation of local and overall hold up in structured packings,[4-9] a film apparatus,[10] a fluidized bed,[11-13] or in a stirred tank reactor.[14] Unfortunately, conventional CT does not allow investigations on a small scale due to its lack of spatial resolution, whereas μCT

overcomes this limitation. μCT is widely used in the field of geological science, for example, for the characterization of the distribution of liquid in porous structures,[15-17] material science, for example, for geometric classification of open-cell material,[18] in biomedical analysis, for example, the investigation of small animals,[19,20] or biology, for example, the investigation of water transport in leaf-like structures.[21] Some effort has been made to reconstruct multiphase interfaces accurately. For example, Andrew et al[22] and Scanziani et al[23] measured contact angles in a porous material, and Santini et al analyzed a droplet that was deposited on a solid surface.[24]

The process of X-ray tomographic imaging consists of different consecutive work steps, which will be explained briefly. The first step is the acquisition of 2D projection images, where scanning parameters, such as the voltage of the X-ray source, the source current and the exposure time affect the quality of the scan.[25,26] The second step is reconstruction. During reconstruction, a 3D data set is generated from the 2D projections. Additionally, disturbances in the reconstructed images, the scanning artifacts, are compensated. A 3D data set consists of a set of sectional slices that consist of 3D voxels. The final step is the post-processing step that starts with the localization and definition of the different phases.

For the distinction between the different phases in the reconstructed images, the segmentation, various approaches exist. As manual thresholding highly depends on the performing person, automated or semi-automated approaches are mandatory for reliable and reproducible results. Eijnatten et al[27] reviewed different image segmentation methods for medical applications under the consideration of segmentation accuracy. Global thresholding uses a lower and an upper gray value threshold to assign voxels with gray values in between to the phase to be segmented. The thresholds can be selected manually or automatically using the Otsu method.[28] The Otsu method selects the thresholds according to statistics of the gray value histogram.[28] However, global thresholding methods tend to fail in capturing interfaces properly, especially when artifacts or image noise limit the quality of an image. Then, manual post-processing is often required.[27] With local thresholding, different thresholds are defined for different regions of interest.[27] Another segmentation approach is the region growing.[29] Starting from a seed point that is placed in the phase of interest, gray values of voxels are compared to gray values of neighboring voxels and assigned to the phase of interest depending on similarity between the neighboring voxel and the growing seed area.[27,29] Additionally, edge detection can be used for image segmentation. Common edge detection methods, such as the Canny edge detection,[30] identify edges based on the gradient in the image.[27] As these methods detect only edges, they have to be combined with other methods to segment phases completely.[27] According to van Eljnatten et al,[27] Canny edge detection based segmentation approaches are one of the most accurate approaches for the segmentation of images that show different contrast in different regions.[27] Additionally, Rathnayaka et al[31] found the Canny edge detection approach to be superior to a single threshold method regarding accuracy and repeatability.[31]

The extension of the micro-computed tomography to multiphase flow in microstructured equipment is novel and poses various challenges besides the presence of typical artifacts. For example, achievable contrast is a bottleneck, especially for liquid–liquid systems, as X-ray attenuation values are often in a similar range for two liquids. Two phases can be distinguished clearly if $\Delta\mu_{signal}/\ \sigma_{signal} > 5$.[26] Therein, $\Delta\mu_{signal}$ is the difference between the mean signals of the phases and σ_{signal} is the standard deviation of the signal. 3D X-ray imaging needs hundreds of 2D X-ray projection images acquired at different rotation angles for successive reconstruction. This can take several minutes to hours and limits the applicability of CT to stationary or highly periodic phenomena. Additionally, evaporation of the liquid must be considered for the investigation of static gas/liquid interfaces.

In this work, we introduce μCT as a useful tool for the investigation of multiphase fluid systems in micro equipment. As the reconstruction and correction of the artifacts are done with the software package *NRecon* (Bruker, Billerica, Massachusetts), which is commercially available, we will only discuss it briefly. Rather the focus is put on the segmentation of the phases. To emphasize the potential of the presented methodology, liquid–liquid and gas–liquid interfaces in thin tubes are scanned and reconstructed. The scanned interfaces are analyzed regarding morphology and wetting behavior. Finally, we discuss the suitability of the presented methodology for the extension of investigations presented in this work to the investigation of multiphase flows in micro equipment.

2 | METHODS AND MATERIALS

2.1 | Experimental set-up

The image acquisition is performed with a Bruker Skyscan 1275 micro X-ray CT system (RJL Micro & Analytic GmbH, Karlsdorf-Neuthard, Germany). The system is equipped with a 10 W maximum power X-ray source with voltages between 20 and 100 kV with a spot size < 5 μ*m*.[32] The distortion-free 3Mp flat panel detector (1,944 × 1,536 pixels) allows isotropic voxel sizes < 4 μ*m*.[32] The scanning chamber permits the mounting of samples with diameters up to 96 mm and heights up to 120 mm.[32] The spatial resolution achieved in a scan results from the distance between the X-ray source and the sample. The shorter the distance between sample and X-ray source the higher is the spatial resolution.

The scanning chamber is shown in Figure 1a) schematically. The sample is placed in the scanning chamber and mounted on the sample holder firmly. During image acquisition, the sample rotates and shadow projections are taken at different angular positions while X-ray source and detector remain fixed. For flow experiments, the Skyscan 1275 is equipped with three fluorinated ethylene propylene (FEP) hoses, which allows fluid supply and removal.

Different thin tubes are filled with oil (PDMS) and deionized water using a syringe, such that a static water–oil interface and a static oil–air interface are formed, see Figure 1b. For the investigation of the water–air interface the tubes are filled with water only, see

Figure 1c. The tubes are sealed with hot glue to avoid evaporation of PDMS or water during image acquisition.

To achieve good contrast between oil and water in image acquisition, liquid polydimethylsiloxane (PDMS, ELBESIL-Öle B, L. Böwing GmbH, Hofheim, Germany, viscosity 9.45 mPas, density 945 $kg\ m^{-3}$) is chosen as the nonaqueous phase. The good X-ray contrast between PDMS and water results from the silicon atom in the molecule structure of PDMS. A rough estimate for the surface tension of PDMS and interfacial tension of PDMS against water is obtained by the extrapolation of values given by Kanellopoulos and Owen,[33] resulting in surface tension of 21.45 $mN\,m^{-1}$ and interfacial tension of 43.2 $mN\,m^{-1}$.

In this work, mainly FEP is used as a tube material. FEP is chemically inert and robust in handling, which makes it a suitable material for investigations on multiphase flow and mass transfer following this work. To investigate the effect of interfacial forces and gravity on the static interface morphology, scans with FEP tubes are performed for two different configurations, see Table 1. In the first configuration, Configuration 1, the tube is oriented upwards, in the second configuration, Configuration 2, the tube is inclined by 45° (Table 1). To test the robustness of the presented methodology, further scans are performed for a smaller tube diameter (d_i = 1 mm) in the upwards oriented configuration.

Additionally, experiments are performed using PMMA (d_i = 1.6 mm) and glass (d_i = 1.7 mm) as the tube material. PMMA and glass are materials commonly used in micro process engineering and well-characterized regarding wetting behavior. This allows quantitative validation of the proposed method. Scans with PMMA and glass are performed in upwards oriented tubes only.

Scans are repeated at least one time to ensure reproducibility. Table 1 gives an overview of the experiments conducted in this work. All experiments are carried out at ambient conditions.

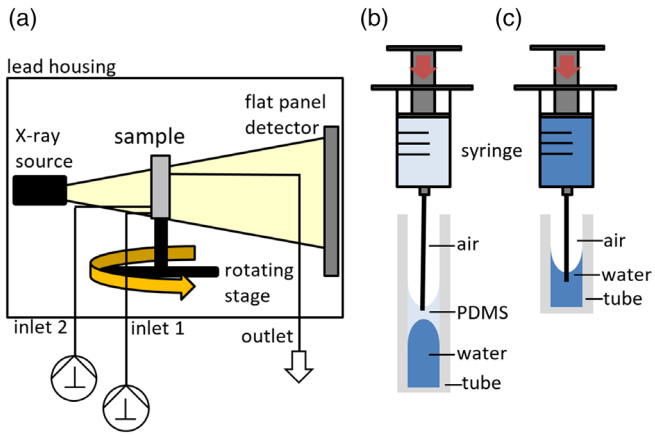

FIGURE 1 (a) Schematic of the experimental X-ray set-up: X-ray source and detector remain fixed while the sample stage is rotated, (b) Filling a thin tube with water, PDMS, and air to obtain an PDMS–air and a water–PDMS interface, (c) Filling a thin tube with water and air to obtain a water–air interface [Color figure can be viewed at wileyonlinelibrary.com]

2.2 | Scanning settings

As the quality of the tomographic images is strongly affected by the imaging process,[26] scanning settings must be chosen carefully. The attenuation of X-rays can be described with Beer–Lambert law (Equation 1).

$$I = I_0 e^{-\mu \cdot \rho \cdot s} \tag{1}$$

In Equation (1) μ is the mass attenuation coefficient, ρ is the density and s describes the thickness of the sample material. Attenuation is always material-specific and additionally depends on the photon energy of the incident beam with the intensity I_0. The maximum energy of a photon E_{max} correlates with the acceleration voltage U_a and the elementary charge e according to Equation 2.[26]

$$E_{max} = e\,U_a \tag{2}$$

Projection images from an FEP tube ($d_i = 1.6\,mm$) partially filled with water, PDMS, and air are acquired at different voltages between 25 and 100 kV. Figure 2 shows the resulting projection images. It can be seen that contrast between the phases enhances with lower source voltages, therefore, with lower photon energy. However, the

TABLE 1 Overview of experiments conducted in this work

Tube material	Investigated interface (fluid at bottom/fluid at top)	Inner tube diameters/mm	Inclination angle/°
FEP	PDMS/air	1/1.6	0/45
FEP	Water/air	1/1.6	0/45
FEP	Water/PDMS	1/1.6	0/45
Glass	PDMS/air	1.7	0
Glass	Water/air	1.7	0
PMMA	PDMS/air	1.6	0
PMMA	Water/PDMS	1.6	0

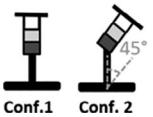

Note: Scans are performed with air, PDMS, and water filled into FEP, PMMA, and glass tubes. For FEP tubes the inner diameter and the inclination angle are varied.

Abbreviations: FEP, fluorinated ethylene propylene; PDMS, polydimethylsiloxane.

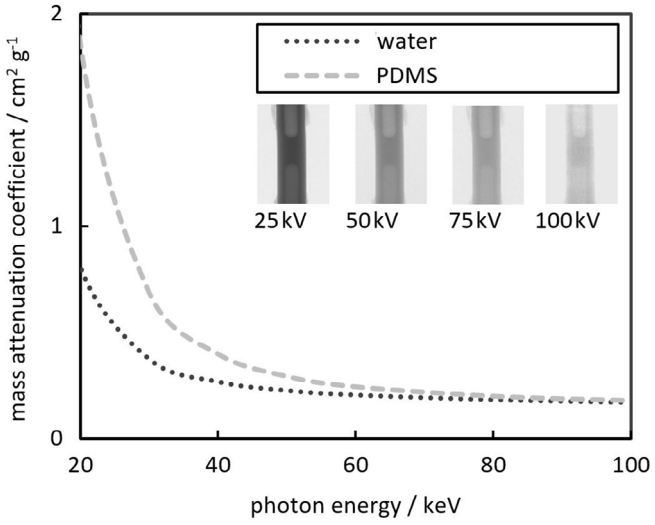

FIGURE 2 Total mass attenuation coefficients for water and PDMS calculated using NIST data[34] and projection images for water, PDMS, and air in an FEP tube (d_i = 1.6 *mm*) acquired at different X-ray source voltages. FEP, fluorinated ethylene propylene; PDMS, polydimethylsiloxane

reduction of the X-ray source voltage, and, hence, the reduction of the mean photon energy, leads to stronger beam hardening,[26] which is explained in the following section.

Apart from contrast, which can be enhanced by choosing an appropriate source voltage, the quality of an image depends on the signal to noise ratio (SNR) (Equation 3). SNR increases with the X-ray dose, which is proportional to the product of source current and exposure time.[26]

$$SNR = \frac{\mu_{signal}}{\sigma_{signal}} = \sqrt{dose} \propto t_{exp} \cdot I_{source} \tag{3}$$

To obtain good contrast and high signal-to-noise ratios in the case of liquid–liquid systems and gas–liquid systems, a low source voltage should be chosen with long exposure time t_{exp} and high source current I_{source} [Equation (3)]. The optimal scan settings depend on the experimental set-up as the tubes serve as filters for the low energy X-rays. This leads to an energy spectrum with increased mean intensity, which affects contrast as demonstrated in Figure 2. In all cases, the source current and exposure time are chosen such that linear detector transmission behavior is guaranteed. For the experiments conducted with glass an aluminum filter is used to enhance the mean intensity of the X-ray spectrum, which reduces beam hardening artifacts. Table 2 shows the settings used for the scans.

2.3 | Post-processing

2.3.1 | Reconstruction and artifacts

The 2D projection images are reconstructed to a 3D data set using *NRecon* that applies the Feldkamp algorithm. This algorithm relies on convolution-back projection for the reconstruction of 3D data from a set of projection images taken at different angular positions.[35] Additionally, artifacts are corrected in *NRecon*. Figure 3 shows a transaxial slice through an FEP tube filled with water and PDMS resulting from reconstruction without artifact correction (left) and with artifact correction (right).

TABLE 2 Scan settings for the investigation of static fluidic interfaces in thin capillaries

Scanning setting	FEP 0°	FEP 45°	Glass	PMMA
Resolution/μm	6.65/8	8–10.47	6.8	8.5
Filter	No	No	Aluminum	No
Voltage/kV	28	35/28	50	35
Current/μA	205	130/205	200	205
Exposure/ms	100/74	120/89	80	75

Abbreviation: FEP, fluorinated ethylene propylene.

Ring artifacts arise from single defect or ill-calibrated detector elements[26] and appear as concentric circles in the reconstructed slices, see Figure 3. Ring artifacts can be reduced in *NRecon*, but not corrected completely in all cases. Thus, even after ring artifact reduction, these artifacts can perturb further post-processing. The misalignment compensation offsets the imperfections of the geometric alignment of the X-ray source, rotation axis, and detector of the image acquisition system.[36] Misalignment causes continuous edges to appear interrupted and locally displaced, see Figure 3. If misalignment is low, misalignment compensation can be done easily using *NRecon*. Another artifact is the beam hardening artifact that is subject to a shift of the energy spectrum of the X-rays introduced by the sample.[26] Beam hardening artifacts are stronger for denser sample materials and lower incident photon energies.[26] Beam hardening is manifested by a decrease of gray values inside a homogeneous phase, as can be seen from the left gray value profile in Figure 3. As can be seen in Figure 3, the low source voltage leads to high beam hardening artifacts. After beam hardening correction, the gray value profile is flattened, see Figure 3 (right). As for this study achieving good contrast is of central interest, little falsification of the gray values caused by the beam hardening correction in the reconstructed slices is tolerated. Finally, the reflection of X-rays can occur. Reflection is visible as dark and bright fields in direct vicinity to the aqueous phase, as can be seen in Figure 3 indicated by the arrows. They are not corrected in this work.

2.3.2 | Image segmentation

In this work, a segmentation routine based on the Canny edge detection is implemented in *MATLAB* (The MathWorks, Inc., Natick, MA). The segmentation process for the extraction of the desired phase from a 3D data set is shown in Figure 4 schematically for the segmentation of water. As depicted in the schematic, some operations are executed in *ImageJ*,[37] an open-source image processing and analysis

tool. To include image processing in *ImageJ* with scripting in *MATLAB*, open-source package *MIJ*[38] is used.

The image acquisition results in a set of X-ray projection images (Figure 4-1). The projection images are reconstructed in *NRecon*, such that a stack of transaxial images (XY) is obtained, see Figure 4-2. Each transaxial image consists of 3D voxels, instead of 2D pixels, that all have a gray value assigned to them. The gray value depends on the mass attenuation coefficient, thus the voxels can be assigned to different phases depending on their gray values. Light materials, such as air, are represented by dark values and dense materials, such as FEP, are represented by brighter shades of gray. The dimension of each voxel in every spatial direction corresponds to the spatial resolution obtained during image acquisition. As a whole, the voxels in all transaxial images represent the entire scanned volume, see Figure 4-13. The transaxial images (XY) show cross-sectional slices along the rotation axis (z-axis) of the image acquisition system. Furthermore, it is possible to contemplate slices from different directions. Slices viewed in the direction of the y-axis are coronal (XZ) slices (Figure 4-3) and slices along the x-axis are sagittal (YZ) slices (Figure 4-4).

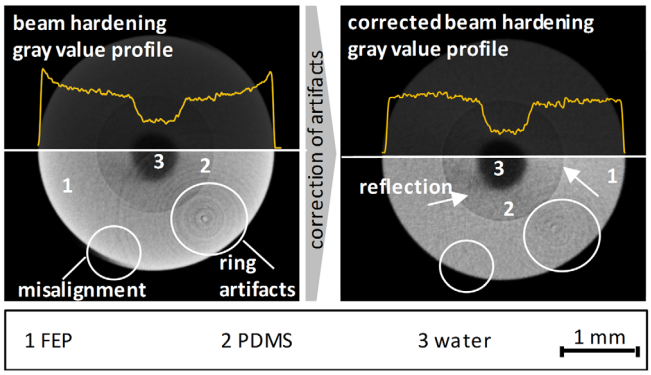

FIGURE 3 Correction of ring artifacts, beam hardening and misalignment in a transaxial slice of an FEP tube (1) filled with PDMS (2), and water (3). On the left, misalignment, ring artifacts and beam hardening are uncorrected, on the right, misalignment and beam hardening are corrected, and ring artifacts are reduced. Reflection artifacts are indicated with the arrows and are not corrected. FEP, fluorinated ethylene propylene; PDMS, polydimethylsiloxane [Color figure can be viewed at wileyonlinelibrary.com]

For the segmentation process, the transaxial stack of images is resliced in *ImageJ* so that an additional stack of coronal (XZ) slices (Figure 4-3) and an additional stack of sagittal slices (YZ) (Figure 4-4) is obtained. In the following steps of the segmentation process, the different stacks are processed in *MATLAB* separately using the segmentation routine described in the following section.

First, edges between the different phases are detected using the Canny edge detection algorithm. The Canny edge detector finds edges according to the maximum gradient magnitude in the images, which are smoothed with a Gauss filter beforehand.[30] It requires three input parameters, a lower and an upper threshold that defines weak and strong edges, and a standard deviation for the Gaussian filter.[39] The appropriate global parameters are found via tuning and should lead to good segmentation results in all slices. If artifacts are strong in

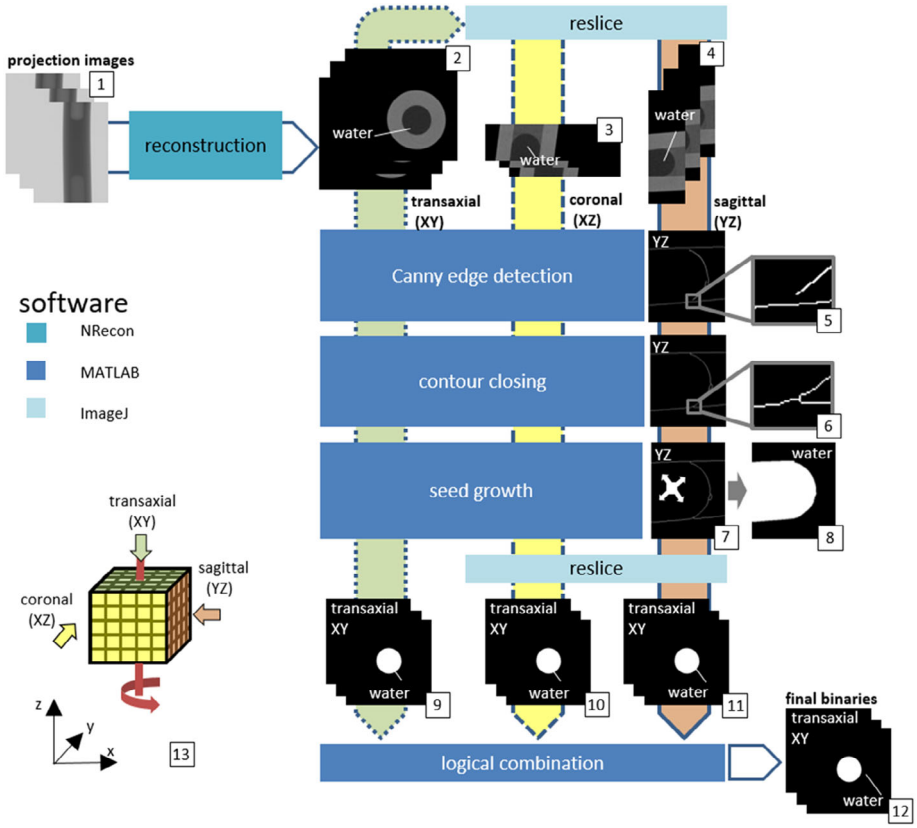

FIGURE 4 Schematic of the segmentation routine based on the Canny edge detection, exemplarily shown for the segmentation of water. Reconstructed images are resliced and transaxial, coronal, and sagittal set of images are segmented in *MATLAB* applying Canny edge detection, contour closing, and seed growth. The different data sets are combined using logical operators to obtain one final transaxial stack of binaries defining the position of water inside the scanned volume [Color figure can be viewed at wileyonlinelibrary.com]

a single slice, the global parameters can be unsuited for the Canny edge detection. In that case, the parameters are adjusted automatically to allow proper segmentation in the relevant slice. Figure 4-5 exemplarily shows the result of the Canny edge detection for a single image from the sagittal stack of slices (YZ). As can be seen in this example, the Canny edge detector fails to produce closed contours. However, for proper segmentation edges must be closed. Therefore, an in-house developed contour closing routine is applied in the following step. For contour closing endpoints of the interrupted edges are identified. The interrupted edges grow together along the largest gradient. Figure 4-6 shows the closed edge after contour closing in the single image from the sagittal stack of slices. After obtaining closed contours, a seed point is defined inside the phase of interest (Figure 4-7) and dilated until it reaches the contours obtained in the previous step (Figure 4-8). Performing seed growth in all images of the transaxial, the coronal, and the sagittal stack results in three sets of binary images, each representing the volume of the phase of interest. In the next step, the binarized coronal stack and the binarized sagittal stack of images are resliced again using *ImageJ* to obtain two different binary transaxial stacks. One stack results from the coronal images (Figure 4-10) and one stack results from the sagittal images (Figure 4-11). The binary transaxial stacks resulting from the coronal and sagittal stack are combined with the original (resulting from stack Figure 4-2) binarized transaxial stack (Figure 4-9) by using expression (4) to obtain the final binarized stack of images (Figure 4-12).

$$[B_{final}] = ([B_{transaxial}]\&[B_{coronal}]) \mid ([B_{transaxial}]\&[B_{sagittal}]) \mid ([B_{sagittal}]\&[B_{coronal}]) \quad (4)$$

Equation (4) states that a voxel is associated with the phase of interest $[B_{final}]$ if the voxel at the same position is assigned to the phase of interest in at least two of three (the transaxial $[B_{transaxial}]$, the coronal $[B_{coronal}]$, and the sagittal $[B_{sagittal}]$) stacks.

As mentioned previously, artifacts are always present in the reconstructed images and prevent the Canny edge detection algorithm to find closed contours or even cause the Canny edge detection algorithm to find unphysical edges, which makes segmentation prone to errors and instabilities. However, artifacts are not pronounced equally in the different sets of stacks. By segmenting the images in different directions and combining the resulting stacks of images using logical operators, as shown in the present work, these difficulties are addressed.

2.3.3 | Performance comparison of different segmentation approaches

As can be seen in Figure 3, the contrast between PDMS and the FEP tube is low. Additionally, ring artifacts and reflection lead to further local deterioration of the contrast between FEP and PDMS. To demonstrate the suitability of the presented image segmentation routine for the application of low contrast segmentation, different segmentation approaches are compared. Therefore, the tube in the vicinity to the water/PDMS interface is segmented using different segmentation approaches, global manual thresholding, thresholding using the Otsu method, and the extended Canny edge detection-based segmentation presented in the previous section. Global manual thresholding and thresholding using the Otsu method are performed in *ctAn* (Bruker, Billerica, MA). For a quantitative comparison of the segmentation approaches the cross-sectional area of the segmented tube is calculated at different transaxial positions and compared to the expected cross-sectional area of the FEP tube (A_{FEP} = 6.03 mm^2).

The results of the performance comparison are shown in Figure 5. The simple global thresholding approach leads to acceptable segmentation results for transaxial positions 0–250 μm. This is the region, where the global upper and lower threshold are adjusted manually such that the tube is segmented correctly. However, above a transaxial position of 250 μm, low contrast, reflection artifacts, and ring artifacts impede the correct segmentation of the tube, which can be seen from the strong deviation of segmented cross-sectional area and expected cross-sectional area. From a transaxial position of 800 μm onwards, the segmented area is ~7.86 mm^2, which is approximately the cross-sectional area of the FEP tube including the void area within.

The Otsu method gives reasonable results, with deviations of a segmented cross-sectional area from the expected cross-sectional area lower than 5% for transaxial positions 0 μm - 400 μm. From a transaxial position of 400 μm onwards, artifacts complicate proper segmentation of the FEP tube, which can be seen from strong deviations between calculated cross-sectional area and expected cross-sectional area.

The extended Canny edge approach presented in this work manages to segment the FEP tube at all transaxial positions with deviations of a segmented cross-sectional area from the expected cross-sectional area lower than 5%.

Both, the manual global thresholding approach and the Otsu method, rely on lower and upper thresholds for the gray values. If gray values are subject to artifacts at certain transaxial positions, as in this work, both methods are not applicable for proper differentiation

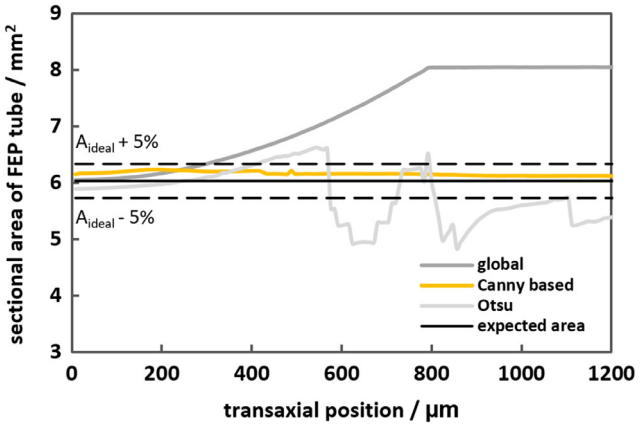

FIGURE 5 Comparison of different segmentation approaches for the segmentation of an FEP tube in the vicinity to the PDMS–water interface. FEP, fluorinated ethylene propylene; PDMS, polydimethylsiloxane [Color figure can be viewed at wileyonlinelibrary.com]

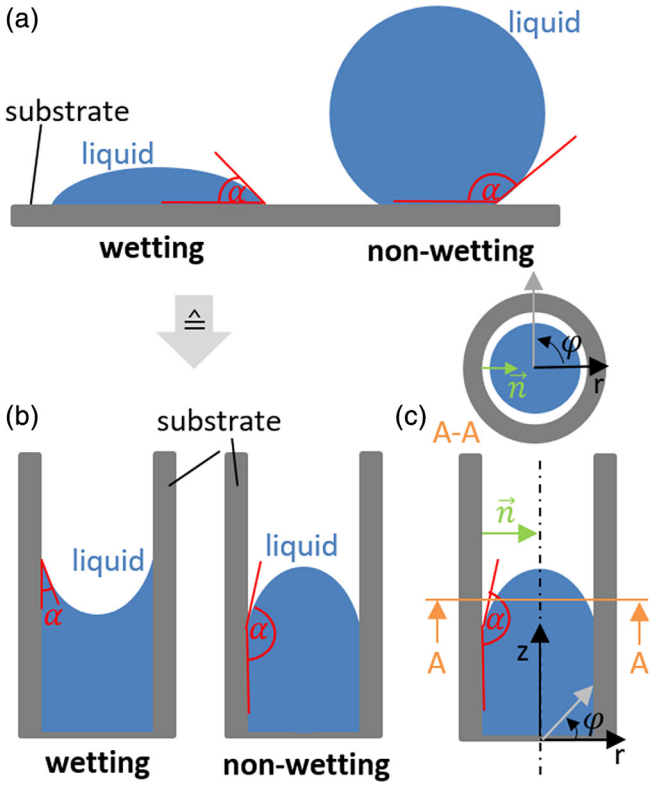

FIGURE 6 (a) Definition of contact angles for a wetting liquid (left) and a nonwetting liquid (right) of droplets placed upon a flat solid substrate, (b) definition of contact angles for a wetting liquid (left) and a nonwetting liquid (right) of liquid filled into a capillary, (c) coordinate system and normal vector for the determination of contact angles in capillaries [Color figure can be viewed at wileyonlinelibrary.com]

between the FEP tube and PDMS, thus, both methods lead to false results for the cross-sectional area of the FEP tube. Furthermore, segmentation results are highly sensitive to the choice of gray value thresholds, which contradicts with automation and reproducibility. In contrast, the Canny edge-based segmentation approach overcomes the issues related to gray value-based segmentation and is applicable even if contrast is very low. The Canny edge segmentation is almost insensitive to user-specified input parameters. This is the basis for the systematic investigation of multiphase interfaces.

2.3.4 | Analysis of extracted fluid interfaces

To give insights into the possibilities emerging with 3D examination using micro CT, the shape of the interface and wetting behavior in different tube materials are exemplarily investigated. Therefore, the x-, y- and z-coordinates of the FEP tube and the coordinates from the interface are extracted from the stacks of binary images.

The data sets are translated and rotated such that the symmetry axis of the tube equals the z-axis of the coordinate system, see Figure 6c). Then, Cartesian coordinates are transformed into cylindrical coordinates using rotational coordinate transformation.

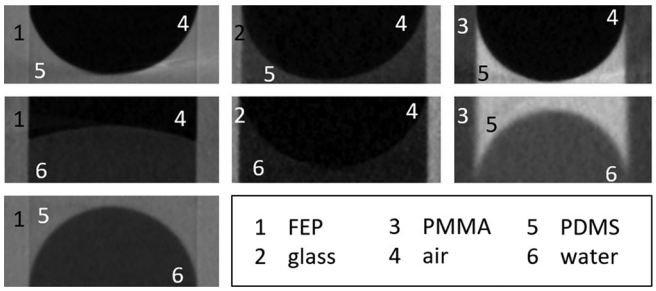

FIGURE 7 Examples for coronal slices after reconstruction: FEP (d_i = 1.6 mm), glass, and PMMA filled with air, PDMS, and water. FEP, fluorinated ethylene propylene; PDMS, polydimethylsiloxane

For qualitative analysis of the interface morphology, the interface is approximated as a sphere using Equation 5.

$$(z-z_0)^2 = r^2 - (x-x_0)^2 - (y-y_0)^2 \tag{5}$$

In Equation (5), x_0, y_0, and z_0 represent the center and r is the radius of the sphere. Both, the origin coordinates and the radius of the approximated sphere are found using a local optimization routine in *MATLAB*.

For the quantitative analysis of the wetting behavior, contact angles are calculated along the circumference of the tubes. Figure 6b shows the definition of the contact angle of liquids in tubes. If the liquid wets the substrate surface, the contact angle is smaller than 90° and the interface is curved downwards. This corresponds to a droplet spreading on a solid surface, Figure 6a. For nonwetting liquids, the contact angle is larger than 90° and the interface is curved upwards, which corresponds to a droplet retaining almost its initial shape when placed upon a flat surface. The contact angle must be measured in the direction normal to the tube surface $\vec{n}$, see Figure 6c. In polar coordinates, this can be done by determining the contact angle for different angular positions φ, if the symmetry axis of the solid tube equals the vertical z-axis, as shown in Figure 6c. In polar coordinates, the interface is approximated as a polynomial $p(r)$ for certain angular positions. The contact angle at different angular positions can be calculated by determining the first order derivative of $p(r)$ at the inner tube diameter ($r = \frac{d_i}{2}$) and calculating the contact angle φ using Equation (6):

$$\varphi = \arctan\left(\left[\frac{dp(r)}{dr}\Big|_{r=\frac{d_i}{2}}\right]^{-1}\right) \tag{6}$$

The approximation of the interface using a polynomial ensures that the effect of data noise on the resulting contact angle is minimized.

3 | RESULTS AND DISCUSSION

3.1 | Reconstructed data sets

Figure 7 shows reconstructed coronal slices that show PDMS–air, water–air, and water–PDMS interfaces in FEP (d_i = 1.6 mm, upright

TABLE 3 Overview about contact angles (mean value and standard deviation) of PDMS in air, water in air and water in PDMS in FEP, glass, and PMMA

Fluids	Settings	Mean/°	*SD*/°
FEP			
PDMS in air	d_i = 1.6 mm, 0°	23.7	3.5
Water in air	d_i = 1.6 mm, 0°	110.3	3.1
Water in PDMS	d_i = 1.6 mm, 0°	162.2	2.5
PDMS in air	d_i = 1.6 mm, 45°	26.8	4.3
Water in air	d_i = 1.6 mm, 45°	102.2	7.2
Water in PDMS	d_i = 1.6 mm, 45°	159.9	2.4
PDMS in air	d_i = 1 mm, 0°	23.4	3.6
Water in air	d_i = 1 mm, 0°	109.8	4.1
Water in PDMS	d_i = 1 mm, 0°	159.0	4.1
Glass			
PDMS in air	d_i = 1.7 mm, 0°	16.1	3.3
Water in air	d_i = 1.7 mm, 0°	34.8	3.3
PMMA			
PDMS in air	d_i = 1.6 mm, 0°	12.9	1.3
Water in PDMS	d_i = 1.6 mm, 0°	156.3	4.4

Note: For each scan, contact angles are measured at 32 positions along the tube circumference. Values given in the table are averages of the measured contact angles determined in all scans.
Abbreviations: FEP, fluorinated ethylene propylene; PDMS, polydimethylsiloxane.

configuration), glass, and PMMA. From Figure 7, wetting and nonwetting phases can be clearly identified from the menisci of the interfaces. In all tubes PDMS can be identified as the wetting phase. Water is nonwetting on FEP but wetting on glass. Apart from these qualitative insights into the wetting behavior, Figure 7 shows the effect of different tube materials on the contrast between different phases. For example, the contrast between PDMS and air is high if scanned inside a PMMA tube compared to the contrast obtained for scanning in FEP, even though scans are performed with the same voltage of the X-ray tube. As FEP has a higher mass attenuation coefficient than PMMA, its filter effect on the mean intensity of the X-ray spectrum is more significant, which explains the lower contrast between PDMS and air in FEP compared to the scan performed in PMMA. This example shows that not only scanning settings but also tube material must be chosen carefully for the design of an experimental set-up for 3D investigation of multiphase flow using CT.

3.2 | Contact angles in different tube materials

As described previously, experiments are performed multiple times independently. Contact angles are determined at 32 positions along the circumference of the tubes for each scan. Table 3 gives mean values and standard deviations for all contact angles measured in FEP, glass, and PMMA.

The contact angle found for water in air at the FEP surface (d_i = 1.6 mm) is 110.3 ± 3.1°. This corresponds well to a value of 111°

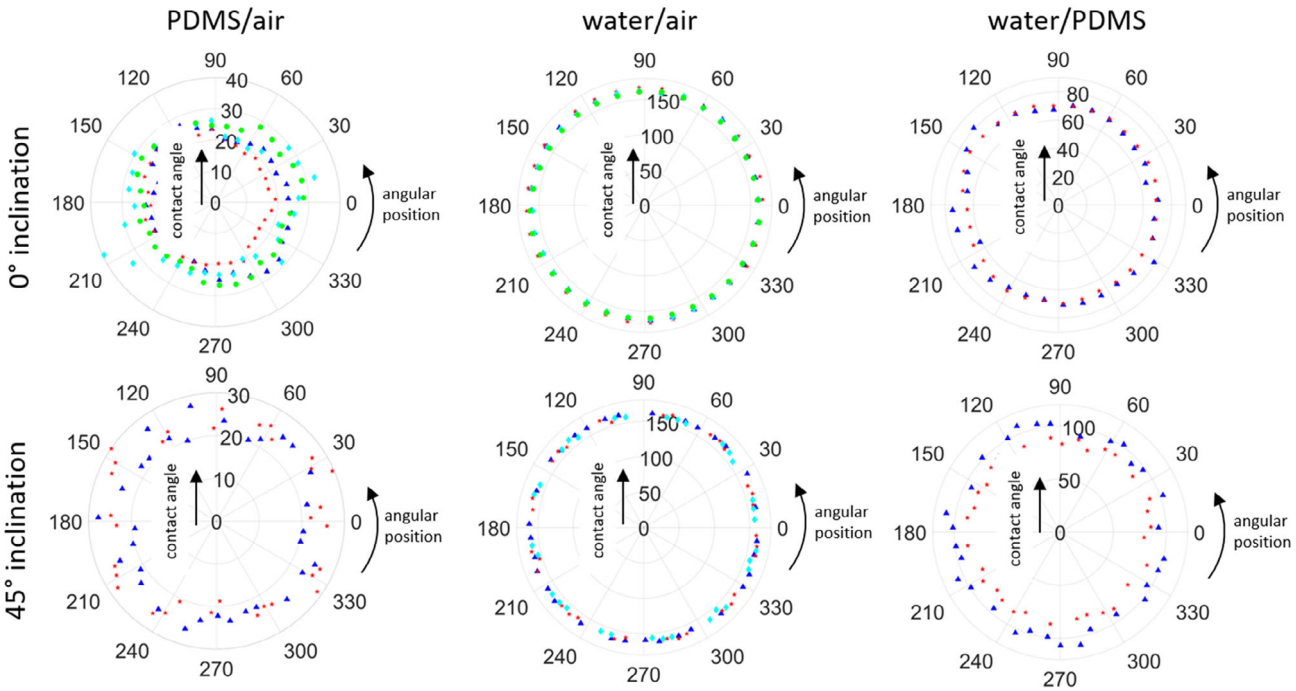

FIGURE 8 Contact angles of PDMS in air, water in air, and water in PDMS along the circumference of FEP tubes (d_i = 1.6 mm) for 0° inclination and 45° inclination. Different markers indicate different scan results. FEP, fluorinated ethylene propylene; PDMS, polydimethylsiloxane [Color figure can be viewed at wileyonlinelibrary.com]

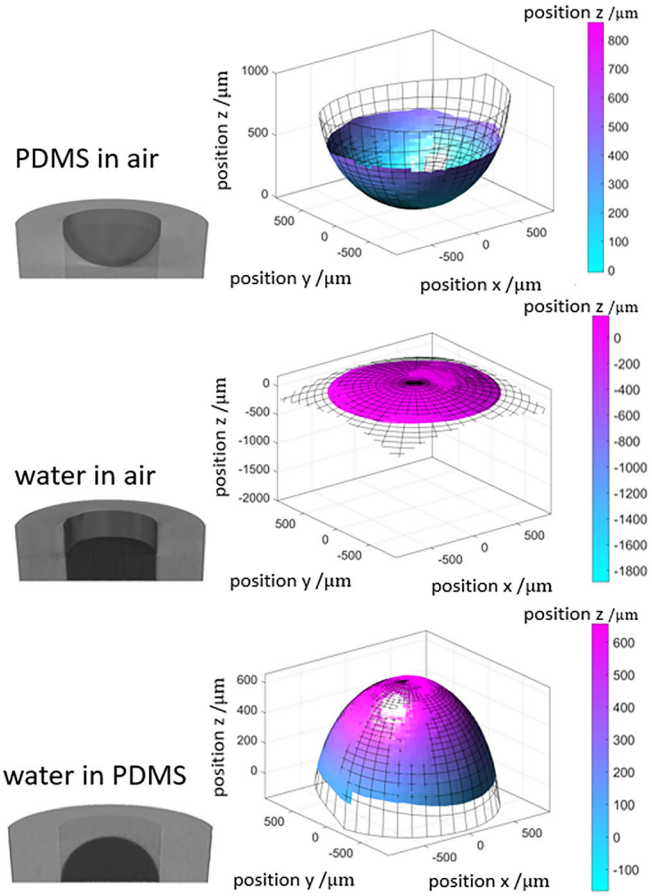

FIGURE 9 3D representations of (*CtVox*, Bruker) PDMS, water and air in an FEP tube (d_i = 1.6 mm) and extracted PDMS–air, water–air, and water–PDMS interfaces superimposed with the ideal spheres (depicted as meshes) found in the sphere approximation. Interfaces extracted from the scans are found to be spherical. FEP, fluorinated ethylene propylene; PDMS, polydimethylsiloxane [Color figure can be viewed at wileyonlinelibrary.com]

found by Ozkan et al.[40] For PDMS in air in the glass tube the contact angle found in this work is 16.1° ± 3.3°, which is only insignificantly higher than the value of 14 ± 2° found by Trinavee et al.[41] For the contact angle of PDMS in air inside the PMMA tube we obtained a value of 12.9° ± 1.3° and thus a slightly higher value than the contact angle of 11° ± 2 found by Trinavee et al.[41] For untreated glass Sumner et al.[42] give a contact angle of water of 32 ± 2°. In this work, the contact angle of water in a glass capillary is found to be 34.8 ± 3.3°.

In general, the contact angles found in this work agree with the contact angles found in the literature. This proves the validity of the presented experimental procedure and post-processing routine. As different tube materials highly affect the resulting contrast in reconstructed data sets (see Figure 2) robustness of the segmentation routine is proved additionally. Comparing contact angles in FEP tubes with an inner diameter of d_i = 1.6 mm with contact angles in the thinner FEP tube (d_i = 1 mm) no significant deviation can be found, which additionally demonstrated the robustness of the presented methodology. However, standard deviations for the contact angles are a bit higher than most standard deviations given for contact angles in literature. As contact angles are highly sensitive to surface contamination and no special treatment of surfaces is done in this work, higher standard deviations found for the contact angles in the present work can be attributed to the experimental procedure rather than the segmentation and post-processing routine.

3.3 | Local contact angles in FEP

Figure 8 shows contact angles for PDMS in air, water in air and water in PDMS in FEP tubes (d_i = 1.6 mm) at different angular positions along the circumference of the tube for 0° inclination and 45° inclination. In the figure, contact angles determined in different scans are marked with different markers. Deviations of contact angles are stronger if comparing the results for different scans than the deviations of contact angles found in one scan. This suggests that the resulting contact angle is more sensitive to the preparation of the tubes than the automated post-processing routine. Comparing results for 0° inclination and 45° inclination no significant differences can be found. Thus, the influence of gravity on the contact angle is found to be negligible.

3.4 | Interface morphology in FEP tube

Figure 9 shows 3D representations after reconstruction of a PDMS/air, a water/air and a water/PDMS interface in an upright oriented FEP tube visualized with *CtVox*, Bruker. Additionally, the interfaces extracted after segmentation are shown and superimposed with the ideal sphere (mesh) that results from the approximation in Equation (5). The surface plots show that the interfaces have nearly spherical shapes.

Body forces and surface forces affect the shape of an interface. However, in miniaturized equipment, surface forces outweigh body forces, such as gravity.[1,2] The interplay of both can be assessed with the Bond number *Bo* (Equation 7), that represents the ratio between body forces and surface forces. It depends on the density difference $\Delta\rho$, the gravity constant g, the hydraulic diameter d_h, and the interfacial tension σ. Usually, surface forces outweigh body forces for hydraulic diameters d_h << 1 mm as described in Günther et al.[2] and Bo << 1, for example, 10^{-4} as described in Kockmann et al.[1]

$$\mathrm{Bo} = \Delta\rho g \frac{d_h^2}{\sigma} \tag{7}$$

For water/PDMS, as for water/air, in the FEP tube (d_i = 1.6 mm), an estimation for the Bond number is 0.03, thus, surface forces are expected to dominate over gravitational forces. For PDMS/air the Bond number is ~1.1, hence, larger than Bo for PDMS–water and water–air. However, as the Bond number is low in both cases, no large deviation between the extracted interface and the ideal sphere can be seen in Figure 9.

To visualize the effect of inclination of the tube on the interface morphology for different Bo, contour plots are generated for the

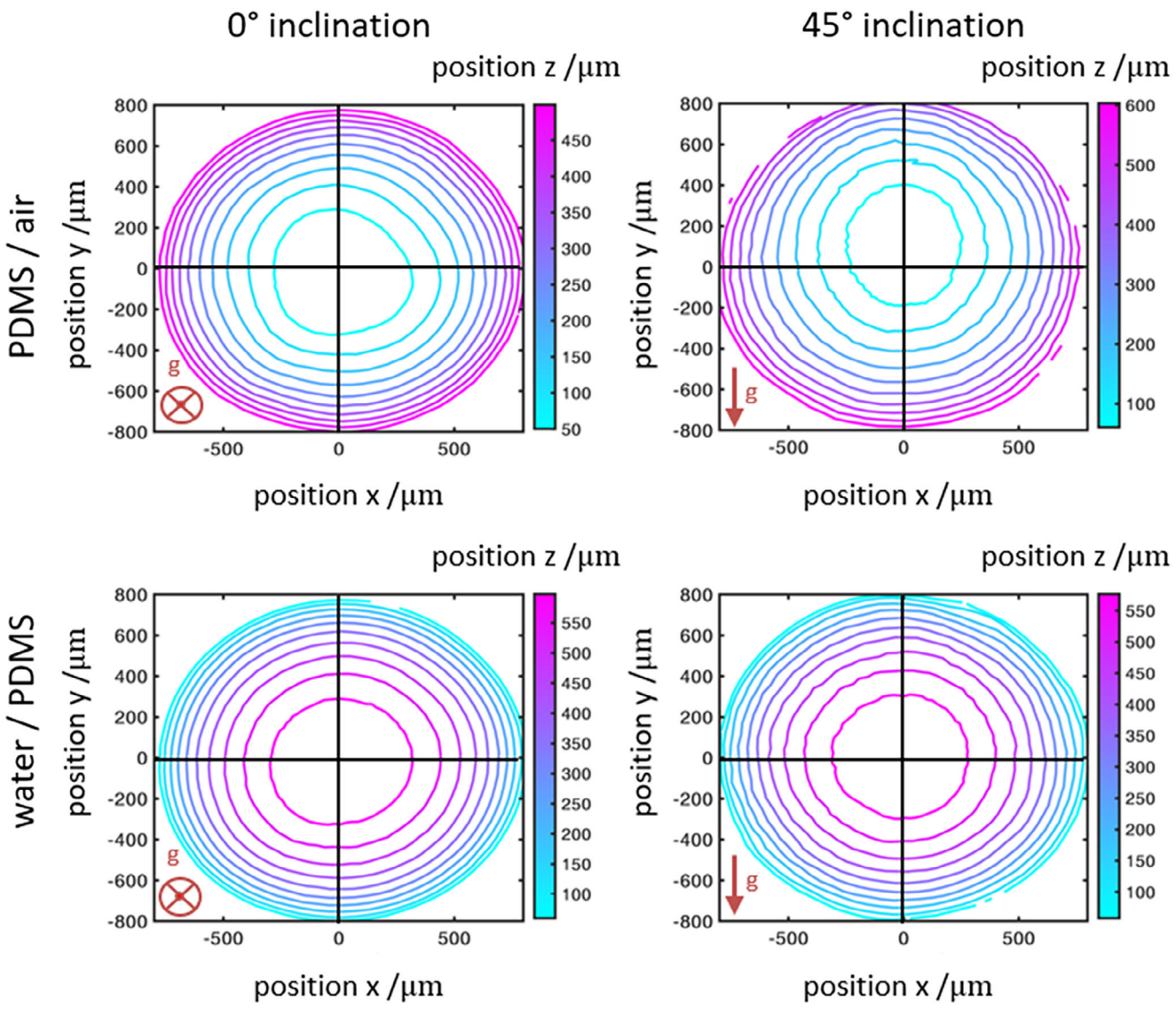

FIGURE 10 Contour plots for the PDMS/air interface and the water/PDMS interface in an FEP tube (d_i = 1.6 mm) for 0° inclination and 45° inclination. The PDMS/air interface shows deformation for the 45° inclined tube due to the influence of gravity. FEP, fluorinated ethylene propylene; PDMS, polydimethylsiloxane [Color figure can be viewed at wileyonlinelibrary.com]

PDMS–air interface (Bo ≈ 1.1) and the water–PDMS interface (Bo ≈ 0.03), see Figure 10. For 0° inclination the isolines, which indicate equal heights, resemble concentric circles with the center at the origin of the coordinate system for both, the PDMS/air interface and the water/PDMS interface. For 45° inclination the contour lines of the PDMS/air interface also resemble concentric circles but with a center shifted in the direction opposite to gravity. As PDMS is denser than air, it is moved in the direction of gravity, whereas air is shifted to the opposite direction. This small deformation of the interface can be detected even for low Bond numbers. As the Bond number is close to one for PDMS and air in the FEP tube both, gravity and interfacial forces affect the formation of the interface, which leads to the deformation found in Figure 10. For PDMS and water the Bond number is 2 orders of magnitudes lower, meaning that gravitational forces contribute more to the morphology of the PDMS–air interface than to the morphology of the PDMS–water and the water–air interfaces. Respectively, no dependency of the deformation of the interface on gravity can be seen in Figure 10.

4 | SUMMARY AND OUTLOOK

In this work, we introduced the method of micro CT for the investigation of multiphase interfaces in microfluidic devices, such as circular capillaries. Therefore, the typical workflow with associated challenges, posed by the different kinds of artifacts and limited spatial resolution, was presented. Special emphasis was given to the segmentation of the different phases as an accurate localization of the interface represents the first step toward a detailed investigation of multiphase interfaces in multiphase flow. We compared different segmentation

approaches and found an in-house developed segmentation routine based on the Canny edge detection to be the only suitable in the presence of strong artifacts and low phase contrast.

In general, contact angles are determined for water, PDMS, and air filled into FEP, PMMA, and glass channels. Contact angles agreed well with values found in the literature, which proofs the validity and robustness of the presented segmentation and analysis approach. Deviations found for the contact angles in the present work are attributed to the experimental procedure rather than the segmentation and post-processing routine. For studies with the scope to systematically investigate contact angles the filling procedure of the tubes with the liquids should be standardized. If done so the proposed methodology could be a good alternative for the determination of contact angles, especially for under liquid wetting, and directly in the miniaturized flow equipment.

To investigate the influence of gravity scans for the larger FEP tube (d_i = 1.6 mm) are performed in two different configurations, in an upwards oriented tube and a tube with an inclination of 45°. Thus, it was possible to identify the contribution of surface forces and gravity to the formation of the PDMS/air interface in the FEP tube with an inner diameter of d_i = 1.6 mm. While gravity has an effect on the interface morphology of the PDMS/air interface in the 45° inclined tube, no effect of gravity on the contact angle could be found.

We found that not only scanning settings but also tube material must be considered carefully when choosing equipment for 3D investigation of multiphase flow. All tested tube materials proofed to be suitable for investigations planned on multiphase flow using μCT. Post-processing can be done with the in-house developed segmentation approach as it proofed to be robust and accurate for the localization of liquid/liquid and gas/liquid interfaces for conditions tested in this work. Therefore, the present work builds the basis for future 3D investigation of multiphase flow regimes in miniaturized equipment, such as slug flow, parallel or annular flow, and droplet generation.

ACKNOWLEDGMENTS

The authors would like to thank the German Research Foundation (DFG, [grant number INST 212/397-1]) that granted the Bruker Skyscan 1275. We acknowledge financial support by German Research Foundation (DFG) and TU Dortmund University within the funding programme Open Access Publishing. Additionally, we would like to thank RJL Micro & Analytic, Karlsdorf-Neuthard, Germany, for technical support and training. Our special thanks go to R. Banerjee, Helmholtz Institute Ulm, Germany, for valuable discussion. Furthermore, we would like to acknowledge, C. Schrömges for valuable discussion and advice and J. Herath for his assistance in performing the experiments.

NOTATION

ROMAN SYMBOLS

A_{FEP}	cross-sectional area of FEP tube (m^2)
Bo	Bond number (–)
d_h	hydraulic diameter (m)
d_i	inner diameter (m)
d_o	outer diameter (m)
e	elementary charge $\left(1.602 \cdot 10^{-19} C\right)$
E_{max}	maximum photon energy (eV)
g	gravity constant (9.81 m s^{-2})
I	intensity ($W\,m^{-2}$)
I_{source}	source current (A)
$p(r)$	polynomial function (m)
r	radius (m)
s	sample thickness (m)
t_{exp}	exposure time (s)
U_a	acceleration voltage (V)
x,y,z	coordinates (m)
x_0, y_0, z_0	center coordinates (m)

GREEK LETTERS

α	contact angle (°)
μ	mass attenuation coefficient ($m^2\ kg^{-1}$)
μ_{signal}	medium value (–)
σ	interfacial tension (N m^{-1})
σ_{signal}	standard deviation (–)
ρ	density ($kg\,m^{-3}$)
φ	angular position (°)

INDICES AND ABBREVIATIONS

CT	computed tomography
μCT	micro-computed tomography
FEP	fluorinated ethylene propylene
PDMS	polydimethylsiloxane
SNR	signal to noise ratio (–)

SYMBOLS AND OPERATORS

&	logical operator (AND)
|	logical operator (OR)

ORCID

Julia Schuler https://orcid.org/0000-0002-0848-0219

REFERENCES

1. Kockmann N. *Transport Phenomena in Micro Process Engineering heat and mass transfer*. Berlin: Springer; 2008.
2. Günther A, Jensen KF. Multiphase microfluidics: from flow characteristics to chemical and materials synthesis. *Lab Chip*. 2006;6:1487-1503.
3. Kockmann N. Transport phenomena and chemical reactions in modular microstructured devices. *Heat Transfer Eng*. 2017;38:1316-1330.
4. Toye D, Marchot P, Crine M, Pelsser A-M, L'Homme G. Local measurements of void fraction and liquid holdup in packed columns using X-ray computed tomography. *Chem Eng Process Process Intensif*. 1998; 37:511-520.
5. Aferka S, Viva A, Brunazzi E, Marchot P, Crine M, Toye D. Tomographic measurement of liquid hold up and effective interfacial area distributions in a column packed with high performance structured packings. *Chem Eng Sci*. 2011;66:3413-3422.
6. Aferka S, Marchot P, Crine M, Toye D. Interfacial area measurement in a catalytic distillation packing using high energy X-ray CT. *Chem Eng Sci*. 2010;65:511-516.
7. Janzen A, Steube J, Aferka S, et al. Investigation of liquid flow morphology inside a structured packing using X-ray tomography. *Chem Eng Sci*. 2013;102:451-460.

8. Calvo S, Beugre D, Crine M, Léonard A, Marchot P, Toye D. Phase distribution measurements in metallic foam packing using X-ray radiography and micro-tomography. *Chem. Eng. Process. Process Intensif.* 2009;48:1030-1039.
9. Schug S, Arlt W. Imaging of fluid dynamics in a structured packing using X-ray computed tomography. *Chem Eng Technol*. 2016;39:1561-1569.
10. Schmit CE, Eldridge RB. Investigation of X-ray imaging of vapor–liquid contactors. 1. Studies involving stationary objects and a simple flow system. *Chem. Eng. Sci*. 2004;59:1255-1266.
11. Maurer S, Wagner EC, van Ommen JR, et al. Influence of vertical internals on a bubbling fluidized bed characterized by X-ray tomography. *Int J Multiphase Flow*. 2015;75:237-249.
12. Bieberle M, Barthel F, Hampel U. Ultrafast X-ray computed tomography for the analysis of gas–solid fluidized beds. *Chemical Engineering Journal*. 2012;189–190:356-363.
13. Mudde RF. Bubbles in a fluidized bed: a fast X-ray scanner. *AIChE J*. 2011;57:2684-2690.
14. Ford JJ, Heindel TJ, Jensen TC, Drake JB. X-ray computed tomography of a gas-sparged stirred-tank reactor. *Chem Eng Sci*. 2008;63:2075-2085.
15. Scanziani A, Singh K, Bultreys T, Bijeljic B, Blunt MJ. In situ characterization of immiscible three-phase flow at the pore scale for a water-wet carbonate rock. *Adv Water Resour*. 2018;121:446-455.
16. Turner ML, Knüfing L, Arns CH, et al. Three-dimensional imaging of multiphase flow in porous media. *Physica A*. 2004;339:166-172.
17. Klise KA, Moriarty D, Yoon H, Karpyn Z. Automated contact angle estimation for three-dimensional X-ray microtomography data. *Adv Water Resour*. 2016;95:152-160.
18. Bock J, Jacobi AM. Geometric classification of open-cell metal foams using X-ray micro-computed tomography. *Mater Charact*. 2013;75:35-43.
19. Holdsworth DW, Thornton MM. Micro-CT in small animal and specimen imaging. *Trends Biotechnol*. 2002;20:S34-S39.
20. Schambach SJ, Bag S, Schilling L, Groden C, Brockmann MA. Application of micro-CT in small animal imaging. *Methods*. 2010;50:2-13.
21. Lee SJ, Kim H, Ahn S. Water transport in porous hydrogel structures analogous to leaf mesophyll cells. *Microfluid Nanofluid*. 2015;18:775-784.
22. Andrew M, Bijeljic B, Blunt MJ. Pore-scale contact angle measurements at reservoir conditions using X-ray microtomography. *Adv Water Resour*. 2014;68:24-31.
23. Scanziani A, Singh K, Blunt MJ, Guadagnini A. Automatic method for estimation of in situ effective contact angle from X-ray micro tomography images of two-phase flow in porous media. *J Colloid Interface Sci*. 2017;496:51-59.
24. Santini M, Guilizzoni M, Fest-Santini S. X-ray computed microtomography for drop shape analysis and contact angle measurement. *J Colloid Interface Sci*. 2013;409:204-210.
25. Morgan TB, Heindel TJ. Sensitivity of X-ray computed tomography measurements of a gas-solid flow to variations in acquisition parameters. *Flow Meas Instrum*. 2017;55:82-90.
26. Buzug T. *Computed tomography*. Berlin: Springer; 2008.
27. van Eijnatten M, van Dijk R, Dobbe J, Streekstra G, Koivisto J, Wolff J. CT image segmentation methods for bone used in medical additive manufacturing. *Med Eng Phys*. 2018;51:6-16.
28. Otsu N. A threshold selection method from gray-level histograms. *IEEE Trans. Syst., Man, Cybern*. 1979;9:62-66.
29. Adams R, Bischof L. Seeded region growing. *IEEE Trans Pattern Anal Machine Intell*. 1994;16:641-647.
30. Canny J. A computational approach to edge detection. *IEEE Trans Pattern Anal Mach Intell*. 1986;8:679-698.
31. Rathnayaka K, Sahama T, Schuetz MA, Schmutz B. Effects of CT image segmentation methods on the accuracy of long bone 3D reconstructions. *Med Eng Phys*. 2011;33:226-233.
32. Bruker Corporation. SkyScan 1275: technical details. https://www.bruker.com/products/microtomography/micro-ct-for-sample-scanning/skyscan-1275/technical-details.html. [].
33. Kanellopoulos AG, Owen MJ. Adsorption of sodium dodecyl Sulphate at the silicone fluid/water Interface. *Trans Faraday Soc*. 1971;67:3127-3138.
34. Hubbel JH, Seltzer S. *Tables of X-ray mass attenuation coefficients and mass energy-absorption coefficients, NIST standard reference database 126*. Gaithersburg, MD: National Institute of Standards and Technology; 1995.
35. Feldkamp LA, Davis LC, Kress J-W. Practical cone-beam algorithm. *J Opt Soc Am A*. 1984;1:612-619.
36. Sun Y, Hou Y, Hu J. Reduction of artifacts induced by misaligned geometry in cone-beam CT. *IEEE Trans Biomed Eng*. 2007;54:1461-1471.
37. Schneider CA, Rasband WS, Eliceiri KW. NIH image to ImageJ: 25 years of image analysis. *Nat Methods*. 2012;9:671-675.
38. Sage D, Prodanov D, Tinevez J-Y, Schindelin J. MIJ: Making Interoperability Between ImageJ and Matlab Possible. ImageJ User & Developer Conference, 24-26 October 2012, Luxembourg
39. Gonzalez RC, Woods RE, Eddins SL. *Digital image processing using MATLAB*. Pearson Prentice Hall: Upper Saddle River, NJ; 2004.
40. Ozkan O, Erbil HY. Interpreting contact angle results under air, water and oil for the same surfaces. *Surf Topogr Metrol Prop*. 2017;5:24002.
41. Trinavee K, Gunda NSK, Mitra SK. Anomalous wetting of underliquid systems: oil drops in water and water drops in oil. *Langmuir*. 2018;34:11695-11705.
42. Sumner AL, Menke EJ, Dubowski Y, et al. The nature of water on surfaces of laboratory systems and implications for heterogeneous chemistry in the troposphere. *Phys Chem Chem Phys*. 2004;6:604.

How to cite this article: Schuler J, Kockmann N. Micro-computed tomography for the investigation of stationary liquid–liquid and liquid–gas interfaces in capillaries. *AIChE J*. 2019;e16890. https://doi.org/10.1002/aic.16890